UKAEA-CCFE-CP(26)31

N. Lonigro, D. M. Kriete, V. Perseo, D. Gradic, F. Henke, M. Krychowiak, F. Reimold, K. Verhaegh

Localizing CIII emission using multi-delay coherence imaging in the W7-X divertor

Localizing CIII emission using multi-delay coherence imaging in the W7-X divertor

N. Lonigro, D. M. Kriete, V. Perseo, D. Gradic, F. Henke, M. Krychowiak, F. Reimold, K. Verhaegh

This paper has been submitted to
6th European Conference on Plasma Diagnostics, Prague, Czech Republic, 7 - 10 Apr 2025

Localizing C III emission using multi-delay Coherence Imaging Spectroscopy on W7-X

N. Lonigro[1,2], D. M. Kriete[3], V. Perseo[4], D. Gradic[4], F. Henke[4], M. Krychowiak[4], F. Reimold[4], K. Verhaegh[5] and the W7-X Team[6],

[1]University of York, Physics dept Plasma Institute, York, United Kingdom
[2]UKAEA, Culham Campus, Abingdon, Oxfordshire,OX14 3DB, United Kingdom
[3] Department of Physics, Auburn University, Auburn, Alabama 36849, USA
[4] Max Planck Institute for Plasma Physics, Greifswald, Mecklenburg-Vorpommern 17491, Germany
[5]Department of Applied Physics, Eindhoven University of Technology, Netherlands
[6] For the full list of the W7-X Team members, see the author list of O. Grulke et al (2024) Nucl. Fusion 64 112002

Keywords: CIS, Coherence Imaging, Zeeman splitting, Wendelstein, W7-X, island divertor

Abstract. Localizing regions of strong spectral emission in the edge of magnetically confined plasmas can give information on where different atomic and molecular processes occur, as well as provide bounds on plasma parameters in those regions. Measurements of 2D spectral emission distributions are available in tokamaks via tomographic inversions, but this is more challenging in stellarators due to the lack of toroidal symmetry. Spectroscopy can provide an alternative way to infer the location of the emission fronts by analyzing the effect of Zeeman splitting on the spectrum for a known magnetic field geometry. As a proof of principle, multi-delay coherence imaging is used to estimate the location of C III emission in the divertor region of the Wendelstein 7-X stellarator for a variety of experimental conditions and magnetic geometries. This allows increased spatial resolution in both poloidal and toroidal directions compared to conventional spectroscopy and could enable reconstructions of the 3D emission distribution in the divertor. Although a significant uncertainty in the precise location is present, the technique is able to differentiate between conditions with the emission close to the target and near the last closed flux surface. To improve the accuracy for future measurements, a new set of crystals is optimized for simultaneous emission location and ion temperature measurements.

1 Introduction

Power and particle exhaust is one of the areas that need addressing to make a fusion power plant viable. Understanding and being able to model the behavior of the plasma in the scrape-off layer of current machines is thus necessary to increase confidence in the extrapolations to reactor conditions. To this end, imaging diagnostics have recently proven valuable in providing 2D information on the plasma state, ranging from electron densities and temperatures [1], particle sources and sinks[2], impurity ion velocities[3][4] and ion temperatures in the core[5] and in the divertor [6].

Inferring the location of *emission fronts*, boundaries of regions with strong spectral line emission, can also be useful in studying the behavior of fusion plasmas. They can give information on the electron temperature, as the emission of a spectral line can drop sharply below an electron temperature threshold, or be used as proxies of physics processes happening in the plasma[7][8][9]. The emission localization can also work synergistically with other spectroscopic measurements, such as impurity ion temperature, allowing to localize these estimates of impurity parameters. Measurements of emission front locations have also been used as sensors in real-time control applications[10][11].

The C III emission front is often used in carbon-walled machines as a simple proxy for the impurity radiation front[12], with a C III emission being peaked at the target suggesting an attached plasma, which becomes progressively more detached as the C III front moves away from the target. Tomographic inversions of filtered visible cameras are often used in tokamaks to localize the carbon emission, relying on the assumption of toroidal symmetry [13][14]. This assumption is clearly broken in stellarators, inherently 3D machines, thus requiring different localization techniques. Due to the low plasma current, the magnetic field geometry is precisely known in the Wendelstein 7-X (W7-X) stellarator[15]. This can allow localizing the line emission of some spectral lines by modeling the effect of Zeeman splitting on the spectrum, thus inferring the magnetic field at the location of emission and ultimately the location itself. This was recently demonstrated using high spectral resolution spectrometers in W7-X [16], allowing inference of the emission location along the lines of sight of the spectrometers, in one poloidal plane of the device. In this work, the possibility to extend this approach to 2D using coherence imaging spectroscopy (CIS) will be investigated, with the goal of studying both poloidal and toroidal variations in the emission location during the transition to detachment.

1.1 Wendelstein 7-X

W7-X [15] [17] is a quasi-isodynamic stellarator based in Greifswald, Germany. The plasma geometry has a 5-fold symmetry, that can be further divided into 10 mirrored half-periods through stellarator symmetry, with a major radius of 5.5 m and a minor radius of 0.5 m. It can be operated in multiple magnetic geometries, allowing studies on the effect of the plasma shape on core and edge properties. It uses an island divertor to manage the heat and particle exhaust from the core [18]. In this divertor concept, resonant magnetic perturbation are induced in the plasma edge to create magnetic islands which act as a buffer between the hot core and the divertor tiles. These intersect 10 discrete divertor modules, each with a vertical and an horizontal target, where the heat flux is deposited. Stable divertor detachment can be induced through radiation of intrinsic impurities alone by increasing the upstream density[19]. It is characterized by an high radiated power fraction, low target peak heat fluxes and a rollover in the particle flux to the target.

Flux surfaces obtained with field line tracing of the three magnetic configurations of interest for this work are shown in figure 1, at a poloidal cross section in the diagnostic field of view. Compared to the standard magnetic configuration, the high-mirror configuration increases the heat load on the vertical target, while the low-iota configuration increases the heat load on the horizontal target. The view of the multi-delay coherence imaging system covers the horizontal and vertical target on the third module lower divertor, with good poloidal coverage for ~ 20 % of a half-period of the plasma configuration ($[131, 138]^{\circ}$). The field of view of the diagnostic is highlighted in blue in figure 2, along with a picture taken by the camera during a discharge in high-mirror configuration overlaid on a CAD view of the in-vessel components.

1.2 Coherence Imaging Spectroscopy

Coherence imaging spectroscopy is an imaging technique that encodes information about the shape of a spectral emission line into a 2D plasma image, thus combining the ability of spectroscopy to infer physics parameters from a spectral line shape with the 2D information of imaging techniques. A polarization interferometer is used to overlay a fringe pattern on the plasma image, which is completely characterized by the *complex degree of coherence* γ. For a narrowband spectrum

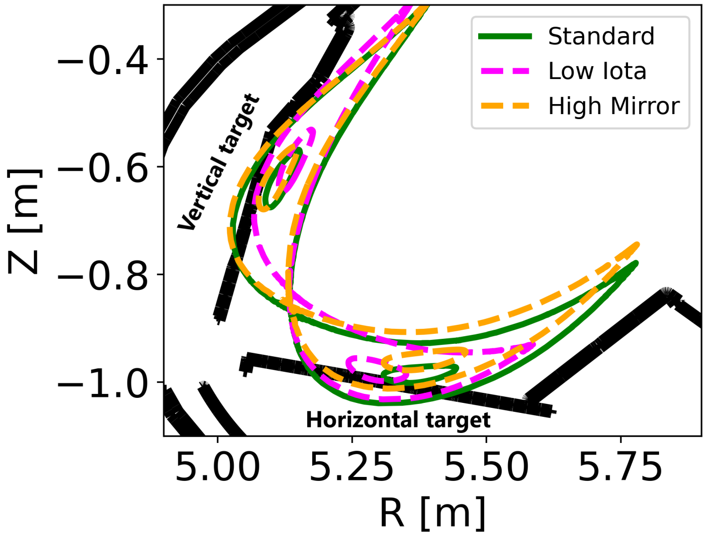

Figure 1: Example island flux surfaces of standard, low-iota and high-mirror configurations for a toroidal angle of 133.5°. Compared to the standard configuration, the high-mirror and low-iota configurations increase the heat load on the vertical and horizontal target, respectively.

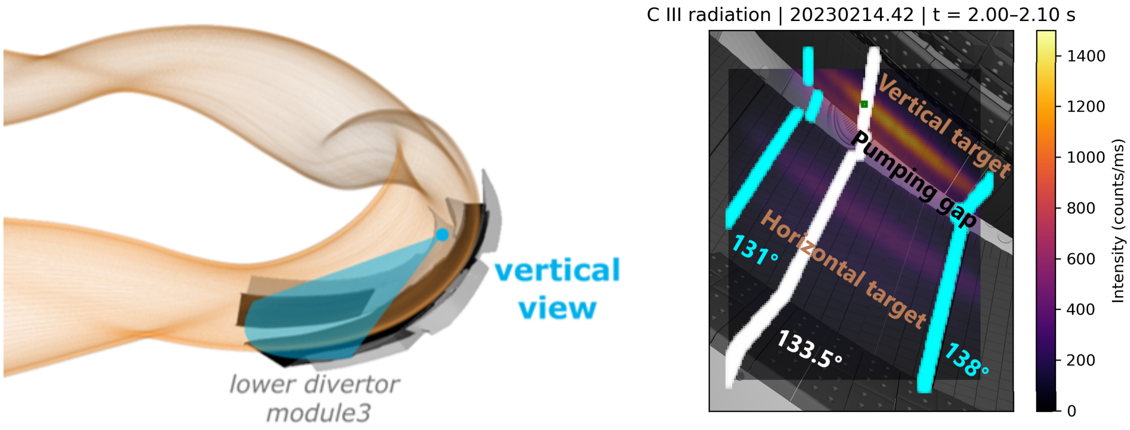

(a) (b)

Figure 2: (a) Plasma last closed flux surface (in orange) of W7-X including a CAD of the divertor module of interest and with the field of view of the diagnostic highlighted in blue. (b) C III Brightness image measured by CIS in high-mirror configuration overlaid on a CAD view of the in-vessel components. The poloidal slice at a toroidal angle of 133.5°, used as reference for the rest of the work, is shown in white while the toroidal angles at 131° and 138°, delimiting the toroidal region with good poloidal coverage, are shown in cyan. The pixel highlighted in green is studied as an example in figure 5 and 6.

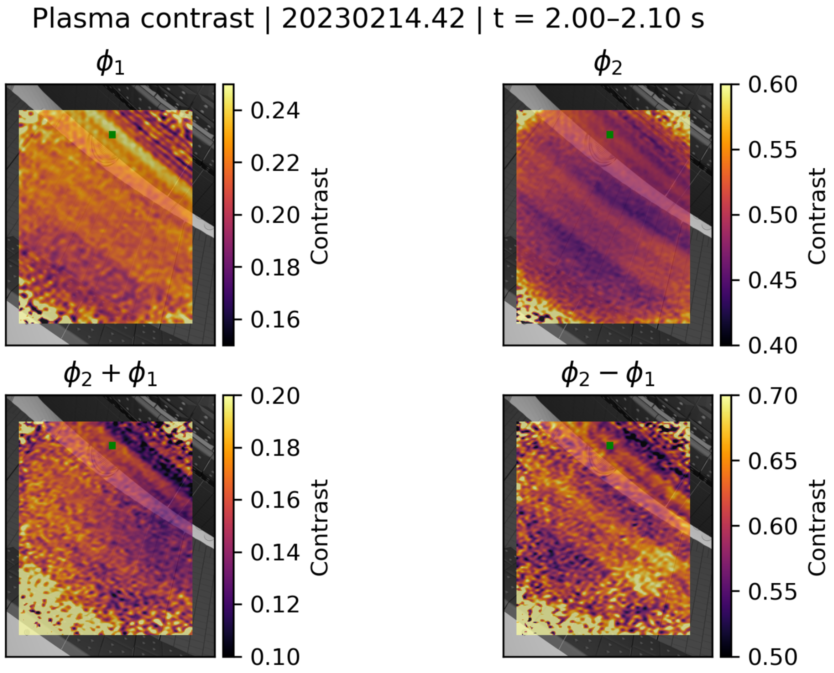

Figure 3: Contrast images measured at the four interferometric delays of the multi-delay CIS system for the same image shown in figure 2b. The pixel highlighted in green is studied as an example in figure 5 and 6. Different colorbars are used for each delay.

($\Delta\nu \ll \nu_0$), γ is linked to the normalized spectrum $g(\nu)$ by

$$\gamma(\phi_0) \approx \int g(\nu) \exp\left(i\phi_0 \left[1 + \kappa_0 \left(\frac{\nu - \nu_0}{\nu_0}\right)\right]\right) \mathrm{d}\nu \tag{1}$$

with ϕ_0 the interferometric delay imparted by the crystals at the frequency ν_0, a design parameter of the instrument, and κ_0 the first-order dispersion of the instrument which can be measured experimentally while calibrating the instrument [20][21]. If the lineshape depends on multiple parameters, for example in the presence of multiple spectral broadening mechanisms, measuring γ at a single value of ϕ_0 may be insufficient as different combinations of multiple parameters may lead to the same γ value. If the broadening mechanisms affect the lineshape differently, they may be distinguished by measuring γ at multiple values of ϕ_0, indexed by j and referred to as ϕ_j in the rest of the work. This can be performed using a multi-delay coherence imaging instrument, which simultaneously overlays multiple interference patterns on the image, which can then be separated in the Fourier domain. Such a system has been used to infer electron densities on Magnum-PSI[22] and MAST-U[23], separating Doppler and Stark broadening, as well as impurity ion temperatures on W7-X[6], where both Zeeman splitting and Doppler broadening must be considered. In addition to the brightness information, as can be obtained with any filtered camera, the experimentally measured quantities related to the shape of the spectrum are the contrast ζ_j and the phase Φ_j for each of the interference patterns, linked to γ_j by

$$\zeta_j = |\gamma_j| \qquad \Phi_j = \arg(\gamma_j) \tag{2}$$

Most of the information on the spectral broadening of the line is contained in the four contrast values. The four contrast images corresponding to the same CIS image shown in figure 2b are shown in figure 3. The possibility of using the current setup of the multi-delay CIS system, described more in detail in [6], for simultaneous inference of ion temperature and emission location will now be investigated.

2 Spectral model

The C III line of interest is the multiplet at 465 nm ($2s3p^3P^0 \rightarrow 2s3s^3S$), which has 3 components corresponding to upper levels with total angular momentum J = 0, 1, 2. The lineshape is given by the convolution of the Doppler broadening component, which depends on the C^{2+} ion temperature T_i, and the Zeeman splitting component, which is influenced by the magnetic field strength (B) and angle between the field and the line of sight (θ). In the presence of impurity flows, the spectrum will also be Doppler shifted and thus dependent on the C^{2+} flow velocity along the line of sight ($\mathbf{v}\cdot\mathbf{l}$). An example of a typical C III spectrum measured in W7-X with the SOPRA high resolution spectrometer looking at the vertical target is given in figure 4[16]. The effect of the Doppler broadening and the Doppler shift on the measured phase and contrast is given by

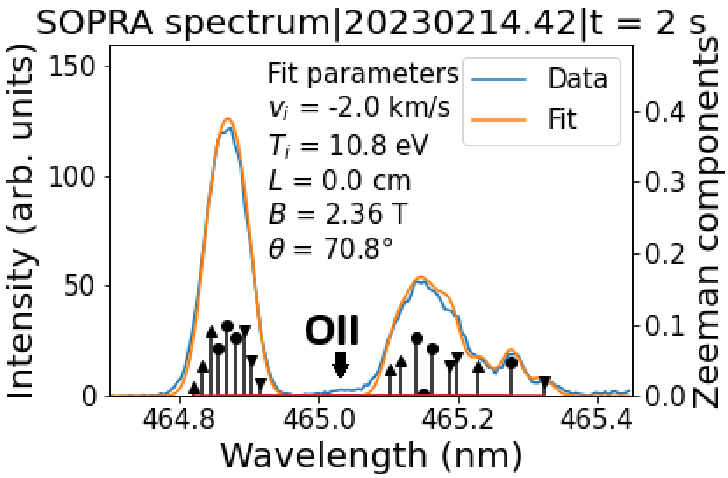

Figure 4: C III spectrum measured and fit with the high resolution spectrometer. The dark lines highlight the π (●), σ^+ (▲) and σ^- (▼) components of the Zeeman splitting. The emission is inferred to be at the target (i.e. zero distance from the plasma facing component along the line of sight, $L = 0$). The contribution from a O II oxygen line contaminating the spectrum is indicated.

$$\zeta_D(\phi_0) = \exp\left(-\frac{T_i}{2m_ic^2}\phi_0^2\kappa_0^2\right) \qquad \frac{\Delta\Phi_D}{\kappa_0\Phi_0} = \frac{\mathbf{v}\cdot\mathbf{l}}{c} \tag{3}$$

with m_i the mass of the ion. The effect of Zeeman splitting and the multiplet structure of the line can be accounted for simultaneously by

$$\gamma_{ZM} = \sum_c A_c \exp\left(i\frac{\kappa_0\phi_0(\lambda_0-\lambda_c)}{\lambda_c}\right) \qquad \zeta_{ZM} = |\gamma_{ZM}| \qquad \Delta\Phi_{ZM} = \arg(\gamma_{ZM}) \tag{4}$$

with A_c and λ_c the normalized amplitude and wavelength of each component of the zeeman-split multiplet. When both effects are significant in the spectrum, the total contrast and phase will be given by

$$\zeta_{DZM} = \zeta_D\zeta_{ZM} \qquad \Delta\Phi_{DZM} = \Delta\Phi_D + \Delta\Phi_{ZM} \tag{5}$$

Additional details of the lineshape model are given in [6].

As the camera view is known and assuming no reflections on the carbon tiles, B and θ are coupled by the requirement that the emission measured by a pixel must be located along its line of sight. Assuming that the C III emission is strongly localized at a single position along the line of sight, they can be joined in the model as a single parameter characterizing the Zeeman splitting (L), which describes the distance from the target along the line of sight where the emission is located. In previous investigations on W7-X it was reported that an enhancement of $\approx 15\%$ in the emission of the J=0 and J=1 states is observed compared to the equilibrium distribution when the divertor is attached [6]. Thus, a possible variation in the multiplet distribution has been added to the model as an additional "multiplet enhancement" parameter (M), which is assumed to be the same for both the J = 0 and J = 1 states. As described in Appendix B, this leads to better results than a fixed M=1 model, which would unrealistically infer the emission to always be detached from the target.

2.1 Limitations of the spectral model

In general, the measured spectral shape will be an emissivity-weighted average of the spectrum along the line of sight and thus dependent on the parameters along the entire line of sight. In this work, a single emission location will be assumed along the line of sight and thus a single set of parameters describing the shape of the spectrum. This assumption is more likely to be appropriate in attached conditions, where the C III emission is more localized close to the target, compared to detached conditions in which the emission is expected to be more distributed through the island[24]. In the case of a distributed emission along the line of sight in a region with weakly changing parameters, the inference values will tend towards their emissivity-weighted average values. Due to the non-linear dependence between the measured contrast and the inferred parameters, the inference will not necessarily result exactly in emissivity-weighted line-averaged parameters and the results will depend on the crystals used, as well as the specific emission and plasma parameters distributions along the line of sight. Similarly, the emission is assumed to be completely produced in the island near the target, and any contribution from outside of the island is neglected. The effects of these assumptions could be explored in future work using synthetic data from EMC3-EIRENE simulations and compared in experiments to tomographic reconstructions of the C III distribution.

The presence of additional impurity lines in the spectrum is neglected, although it can effect the lineshape and thus the measured contrast and phase values. This highlights the complementarity of CIS and dispersive spectroscopy techniques, which can be used to monitor the presence of unaccounted for spectral features in the CIS signal. The effect of these additional O II oxygen line on the contrast is a multiplication factor for each of the 4 contrast values $\xi_{O,j}$ [6]. Future work could focus on including correction values obtained from the dispersive spectrometers to remove this undesired contribution. Alternatively, if the emission location and impurity ion temperature are assumed to be the same between the two emitting species, $\xi_{O,j}$ only depends on the relative strength of the oxygen and carbon line emission and it might be possible to infer it using CIS. A comparison of the results using with a model which includes an O II oxygen impurity line in the spectrum as a fifth parameter is given in Appendix B. With the current CIS setup, the emission is inferred to always be localized at the target when including the oxygen emission fraction as a parameter, suggesting that not enough spectral information is encoded in the current 4 contrast values to infer the oxygen concentration, and thus a negligible oxygen contamination is assumed. These improvements to the spectral model, coupled to an optimized crystal set for Zeeman localization measurements (discussed in section 7), could improve the localization performance and possibly allow more quantitative studies on the emission location.

3 Bayesian parameter inference

The analysis is performed using a grid-based Bayesian approach on each pixel independently. The degree of coherence γ is computed on a 4D grid of parameters (T_i, L, v, M) using equation 1 for each of the 4 delays ϕ_j, measured for each pixel during the calibration. The likelihood of each point on the grid is then computed by comparing the experimentally measured contrasts ζ_j and phases Φ_j to the modeled values $\zeta_j^\star(T_i, v, L, M) = |\gamma_j(T_i, v, L, M)|$ and $\Phi_j^\star(T_i, v, L, M) = \arg\gamma_j(T_i, v, L, M)$, in the assumption of a Gaussian uncertainty distribution

$$\mathcal{L}(T_i, v, L, M) = \prod_j \exp\left\{-\frac{1}{2\sigma_{\zeta,j}^2}\left[\zeta_j - \zeta_j^\star(T_i, v, L, M)\right]^2\right\}\exp\left\{-\frac{1}{2\sigma_{\phi,j}^2}\left[\phi_j - \phi_j^\star(T_i, v, L, M)\right]^2\right\} \tag{6}$$

The posterior distribution can be computed according to Bayes' theorem by multiplying the likelihood distribution by the prior distribution $p(T_i, v, L, M)$ and normalizing by $p(\zeta, \phi) = \int\int\int\int \mathcal{L}(T_i, v, L, M)\, p(T_i, v, L, M)\, \mathrm{d}T_i \mathrm{d}v \mathrm{d}L \mathrm{d}M$:

$$p(T_i, v, L, M|\zeta, \phi) = \frac{\mathcal{L}(T_i, v, L, M)\, p(T_i, v, L, M)}{p(\zeta, \phi)} \tag{7}$$

The prior distribution is taken to be the product of 4 independent probability distributions on each parameter, uniform in the following intervals and zero outside of them

$$T_i \in [0, 30]\ eV \qquad L \in [0, L_{LCFS} + 0.1]\ m$$
$$v \in [-10, 10]\ km/s \qquad M \in [0.9, 1.15]$$

with L_{LCFS} the distance of the last closed flux surface (LCFS) from the target along the line of sight of each pixel, thus restricting the emission location to be between the target and 10 cm inside of the LCFS. The procedure for determining L_{LCFS} is laid out in Appendix A. The result is a probability distribution function (PDF) for each pixel over the four-dimensional parameter space, which can be marginalized to obtain probability distributions for a subset of the parameters. 2D PDFs over T_i and L can be obtained by marginalizing over the velocity and multiplet weight dimensions

$$p(T_i, L|\zeta, \phi) = \int\int p(T_i, v, L, M|\zeta, \phi)\, \mathrm{d}v \mathrm{d}M \tag{8}$$

Example 2D PDFs are shown in figure 5 for a pixel looking at the strike line on the vertical target (indicated in green in figure 2b) in attached and detached conditions for the same discharge as in figure 3. The correlation between the two variables can be noticed as a tilt in the region of high probability space and will be discussed further in section 4. 1D PDFs for each parameter can analogously be obtained by integrating over all the other dimensions. The uncertainty on the inference of each parameter is then estimated as the symmetric 68 % interval of the 1D PDF around the *maximum a posteriori* (MAP) of the marginalized distribution. Example marginalized PDFs for L for the same pixel as in figure 5 are shown in figure 6, as the emission moves from the target to the LCFS, along with the inferred uncertainty of the inferred location.

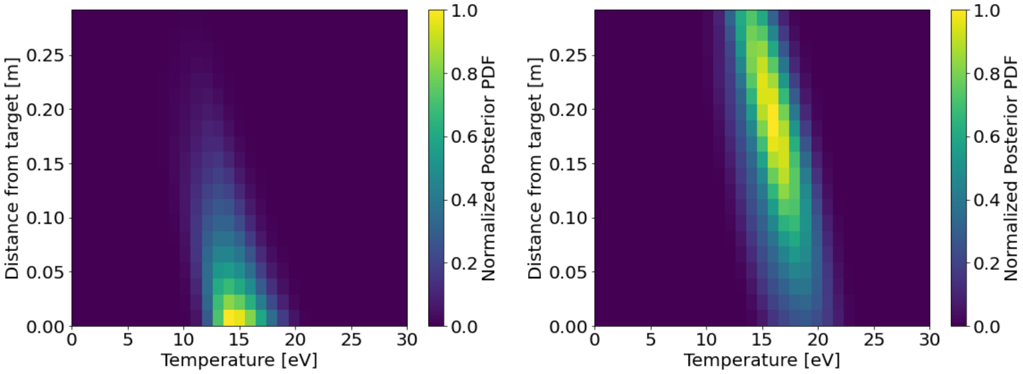

(a)

(b)

Figure 5: PDF of T_i and L for a pixel looking at the strike line on the vertical target, highlighted in figure 2, in attached (a, t = 2 s) and detached (b, t = 6 s) conditions of discharge (#20230214.42) in the high-mirror configuration.

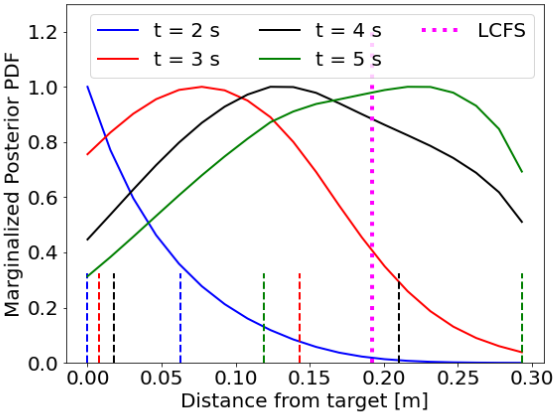

Figure 6: Marginalized PDF for the distance from the target along the line of sight for a pixel looking at the strike line on the vertical target, highlighted in figure 2b, ranging between when the emission is at the target (t = 2 s) and close to the LCFS (t = 5 s) in discharge #20230214.42. The area between the vertical bars shows the region of parameter space within a 68% uncertainty interval.

A large uncertainty is inferred on the location along the line of sight, especially once the emission moves off the target, which can cover more than half of the allowed location range. Thus, precise inferences of the location along the line of sight based on data from a single pixel appear beyond the capability of the current system. Nevertheless, inferences based on a single pixel may still be useful as a binary indicator of the emission being peaked at the target or in the island, thus a proxy for attached or detached conditions. If the error on the measured contrast has no bias, improved inferences could also be obtained by lowering the uncertainty through spatial and temporal averages. In section 5 and 6, the inference will be compared against other diagnostics in different operating conditions, mostly to qualify it as a binary predictor of detached conditions, while an improved set of crystals optimized for Zeeman localization will be described in section 7.

The residuals of the analysis, expressed as a relative percentage deviation of the most likely modelled contrast from the measured values, are shown over the entire image for the four delay values in figure 7. The presence of a bias in the residuals suggests that the deviation from experimental values is not purely due to noise in the measurement but to either a systematic error in the instrument calibration, interferogram demodulation error, or a deficiency in the spectral model.

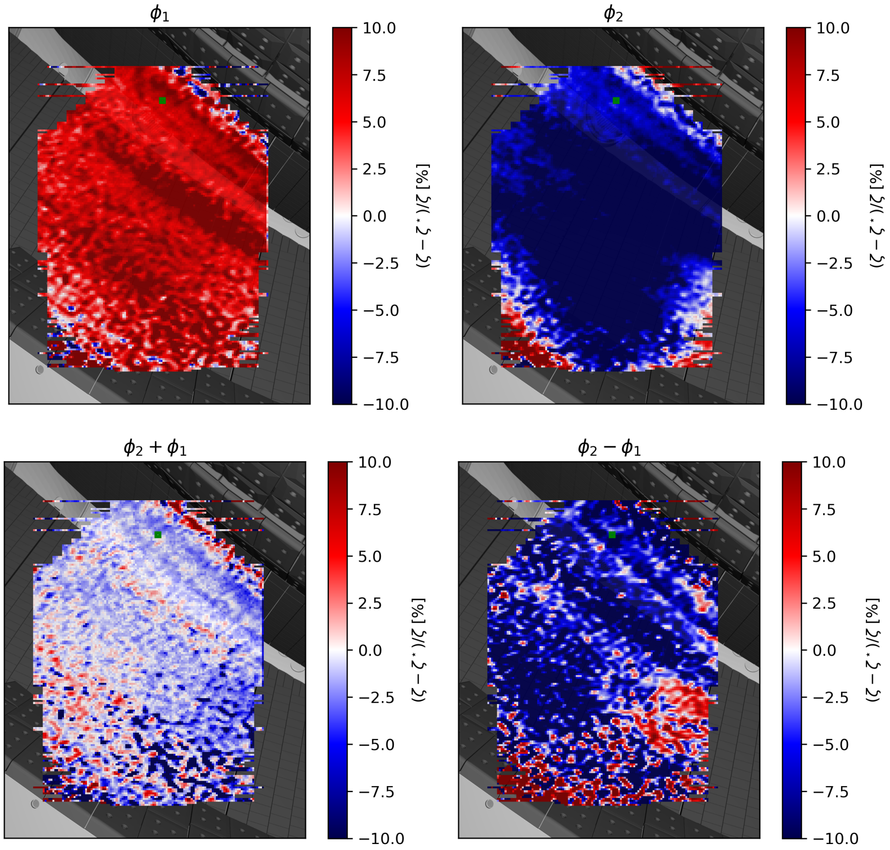

Figure 7: Residuals for the 4 contrast values at $t = 2$ s in discharge #20230214.42, expressed as a percentage of the measured value. The pixel highlighted in green is studied as an example in figure 5 and 6.

Smaller residuals are found on the vertical target, where the best performance is expected, as discussed in section 4. The residuals are also smallest for the $\phi_2 + \phi_1$ delay, which encodes most of the information on the C III location, also discussed in section 4.

4 Contrast sensitivity to Zeeman splitting

Given the known camera view and magnetic geometry of W7-X, it is instructive to study the expected variation of the measured contrast due to Zeeman splitting for different emission locations between the LCFS and the target, and compare it to the uncertainty in the measurements. The average gradient in the magnetic field strength along the lines of sight between the LCFS and the target is shown for the standard W7-X magnetic configuration in figure 8, along with the difference in magnetic field between the LCFS and the target. The sign of the magnetic field gradient is different between the left and right sides of the image, with $|B|$ increasing toward the target on the right and decreasing toward the target on the left. In some regions of the image, the magnetic field strength can be non-mononotic along the line of sight of the pixel, possibly due to the coil ripple. These regions have been masked-off.

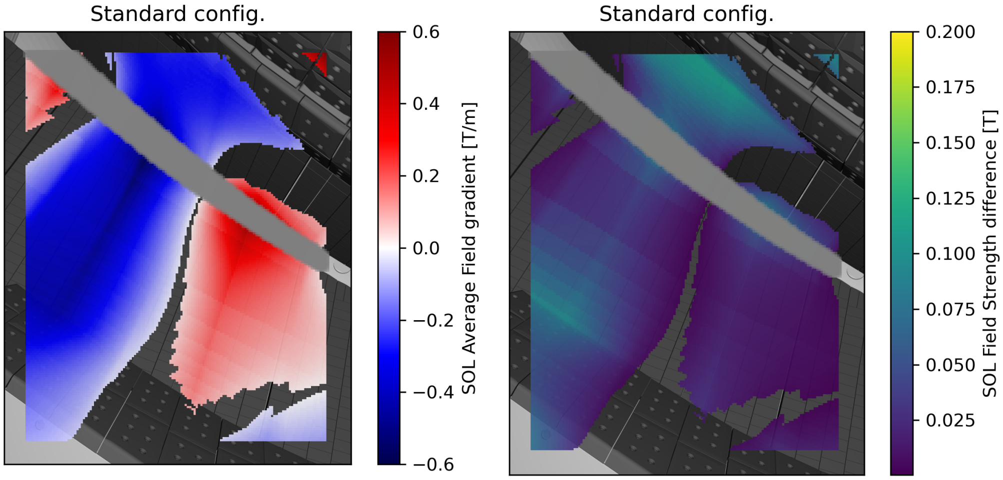

(a) (b)

Figure 8: (a) Average magnetic field strength gradient and (b) difference in magnetic field between the LCFS and the target along the lines of sight in standard magnetic configuration. The pumping gap is masked off in gray and the region where the field is not monotonic is not plotted.

The different sign of the gradient could be useful in suggesting the presence of systematic errors in the inference, as they could shift the inferred emission in different directions along the line of sight in the two halves of the image, with respect to the correct value. Furthermore, the correlation between the variables in figure 5 can then be interpreted as a correct inference of the total amount of broadening, but an uncertainty on how much of this broadening can be attributed to Zeeman splitting versus Doppler broadening, which propagates in the analysis from the initial uncertainty in the measured contrast. Both the magnetic field gradient and the absolute difference in magnetic field are larger on the left part of the image compared to the right, suggesting that better inference performance is expected in the former. Lastly, while the gradient is slightly larger on the horizontal target, the absolute difference is much larger on the vertical one. This is due to the larger distance between the LCFS and the divertor tiles for the pixels looking at the vertical target and it is a feature of the magnetic geometry and camera position. The best performance is then expected in the top left of the image, corresponding to the vertical target.

By comparison, the absolute magnetic field difference for the low-iota and high-mirror magnetic configurations are also shown in figure 9. The field difference is seen to be the lowest in the low-iota configuration and increasingly larger in the standard configuration and in the high -mirror configuration, suggesting that the best inference performance will be obtained in the latter.

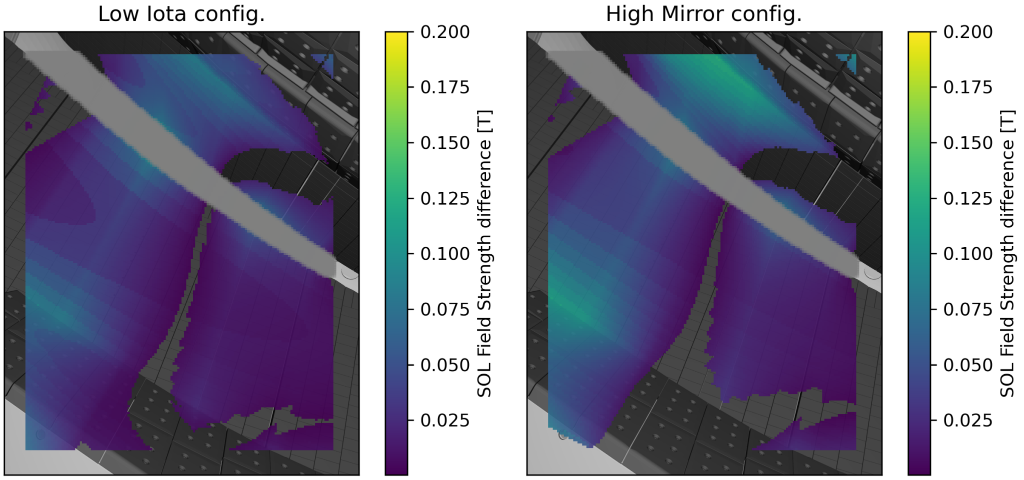

(a) (b)

Figure 9: Variation of the magnetic field strength between the LCFS and the target in low-iota (a) and high-mirror (b). The pumping gap is masked off in gray and the region where the field is not monotonic is not plotted.

Assuming a representative ion temperature of 10 eV and no enhancement in the multiplet emission (M = 1), the relative contrast variation between the emission at the LCFS and at the target is shown for the two most sensitive contrast terms in figure 10 for the high-mirror configuration. Typical uncertainties in the contrast measurements are of 2 %, thus suggesting that most of the information on the location of the emission is contained in the sum term $\phi_2 + \phi_1$, while the other terms will mostly be used to constrain the other lineshape parameters.

5 Proof of principle: detecting the C III front movement in a discharge with strong line-averaged density oscillations

To test the emission localization, the inference was applied to a discharge in the standard configuration with a strongly oscillating line-averaged density (#20221206.46), cropping the image to the region with good signal. In this discharge, the divertor starts in attached conditions and then

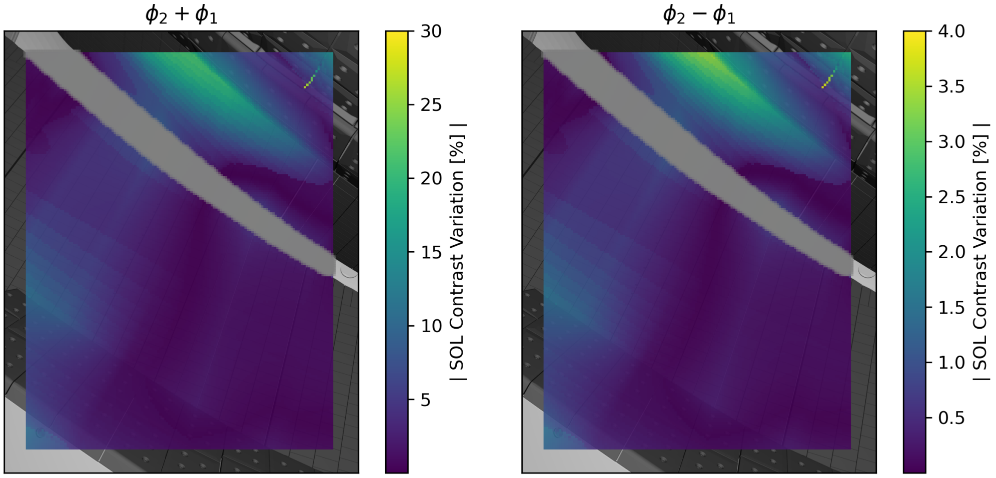

Figure 10: Absolute variation of the contrast between the emission at the LCFS and the target in the high-mirror configuration, plotted using different colorbar ranges for the two most sensitive contrast terms. The pumping gap is masked off in gray.

oscillates strongly between the detached and attached state along with the line-averaged density. The C III brightness images observed by a toroidal camera view at the minimum and maximum of the oscillation are shown in figure 11, where the emission can be seen to move inward in the detached phase.

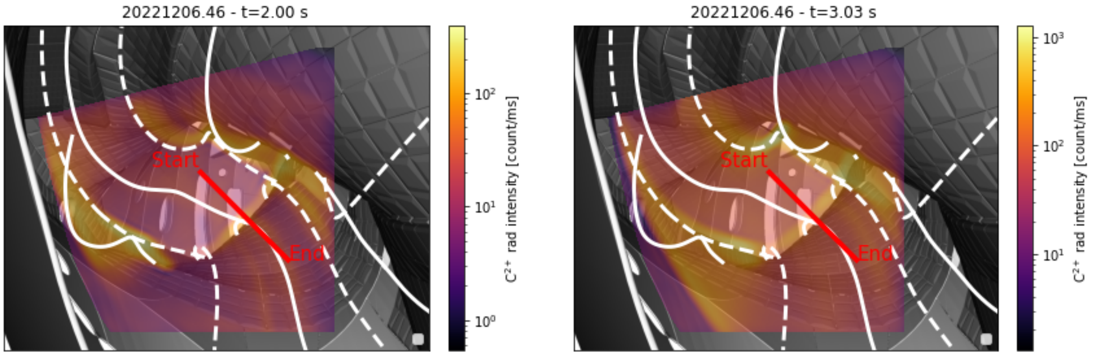

(a) (b)

Figure 11: C III brightness images measured by the toroidal CIS view in the attached (a) and detached (b) oscillation phase of discharge #20221206.46, where the C III emission has moved inward towards the core. The dashed white lines are projections of the island X-points (regions between different islands) and the solid lines are projections of the O-points (center of the islands). Movement of the emission along the red line is used for qualitative comparisons to the CIS inferred location in section 6.

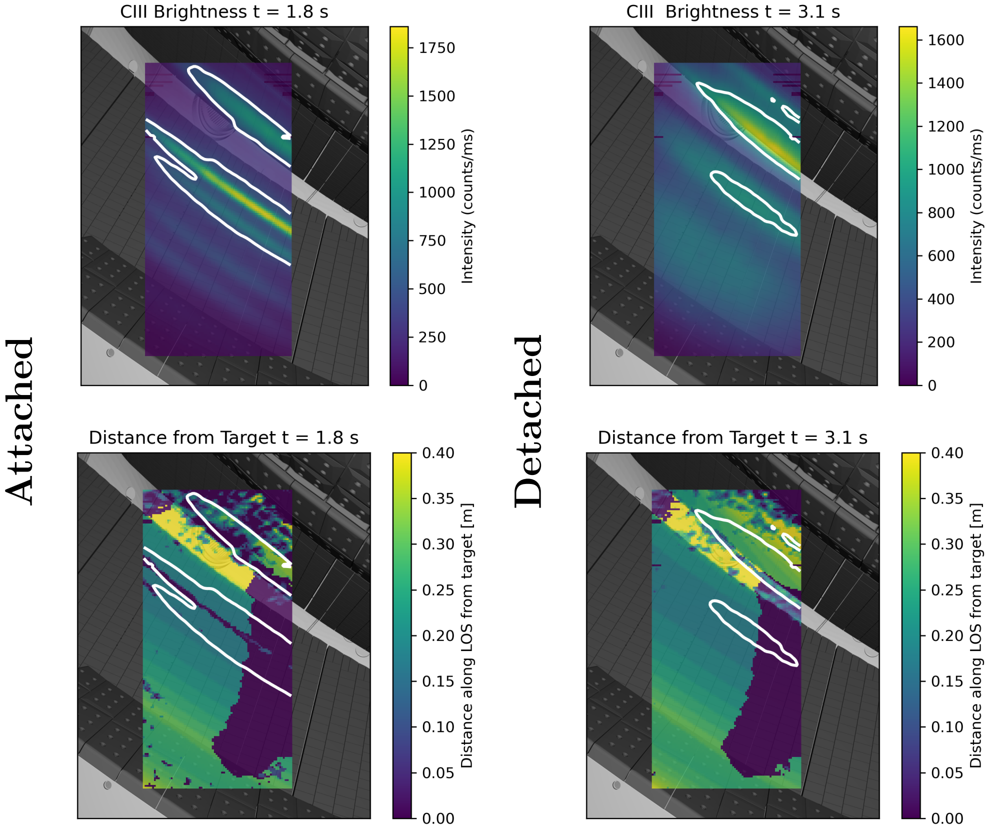

Figure 12: Brightness and MAP of the distance from the target along the line of sight in the attached (1.8 s) and detached (3.1 s) phase of the plasma (#20221206.46). Countor lines at 25 % and 50 % of the maximum brightness are shown as white lines in the attached and detached case respectively.

The C III image brightness and the MAP of the distance from the target are shown before the start of the oscillation in line-averaged density and during a peak in line-averaged density in figure 12. The emission on the vertical target is inferred to initially be closer to the target, and then move away from it in the detached phase, as it would be expected. On the horizontal target, instead, the emission is always inferred to be away from the target for most of the left part of the image and always is attached on the right. The only response is observed for a small band, slightly below the main brightest emission band. This suggests that the analysis is not accurate enough to infer the location for the emission on the horizontal target, at least in the standard configuration, probably due to the smaller variation in magnetic field compared to the vertical target. The stark difference between the left and right part of the horizontal target might also be indicative of a spectral feature unaccounted for in the model, as it would appear that the inference tries to push the inferred location to region of higher magnetic field, which points in the opposite direction in the two halves of the image (figure 8a). Some possibilities could be the presence of oxygen impurities

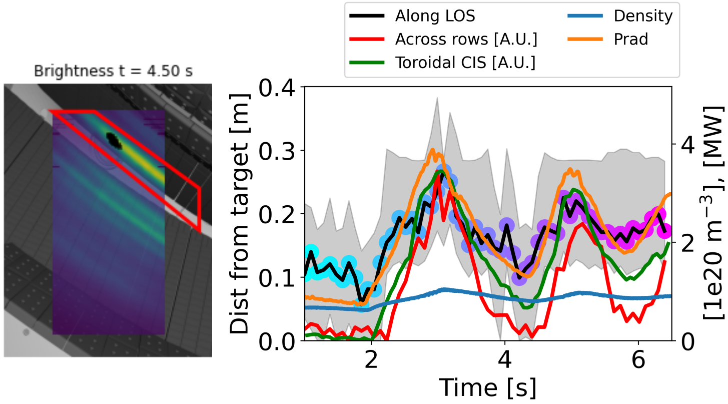

(a) (b)

Figure 13: (a) Example region of interest for the vertical target (red polygon) in discharge #20221206.46 at time t = 4.5 s (attached conditions). The 25% brightest pixels in the region of interest with inferred location in the toroidal range [133.3, 133.8]° are highlighted in black. (b) Evolution of the average MAP of the distance from the target for the black pixels, with uncertainty shaded in black. Also shown are the line-averaged density, the radiated power, the movement of the peak brightness across image rows and the movement of the emission peak along the reference line in figure 11, both normalized with a minimum in 0 and maximum corresponding to the maximum value of the average MAP.

in the spectrum, further discussed in Appendix B, or the lower magnetic field variation on the right part of the image, as discussed in section 4.

The movement of one of the emission bands in a poloidal plane can be followed by using a polygon mask (shown in red in figure 13) to select the emission band of interest, applying a filter on the toroidal angle of the inferred emission, and then plotting the average position of the brightest pixels($\geq$ 75% of the maximum emission in the red mask).

The average MAP distance from the target for these filtered pixels with inferred emission location in the toroidal range [133.3, 133.8]° is shown in figure 13, along with the line-averaged density trace from the interferometer and the radiated power trace from the bolometers[25]. The PDF for this quantity is obtained as the sum of the PDFs of the individual pixels. The *mostly radial* change in distance from the target along the line of sight can be compared qualitatively to:

- The *mostly poloidal* movement of the peak brightness across the camera rows, rescaled to have the minimum in 0 and the maximum to the maximum distance inferred by the multi-delay CIS. If the C III emission is well localized and, as expected from EMC3-EIRENE simulations in standard configuration[24], the movement is predominantly along the separatrix of the magnetic island, the emission would be expected to move away from its initial position at similar times in both the poloidal and radial directions. The two directions of movement are compared in figure 14.
- The movement of the peak emission observed by the toroidal CIS system along the selected line in figure 11, which is mostly radial, rescaled to have the minimum corresponding to 0 and the maximum to the maximum distance inferred by the multi-delay CIS.

The inferred distance from the vertical target is seen to oscillate following the radiated power trace

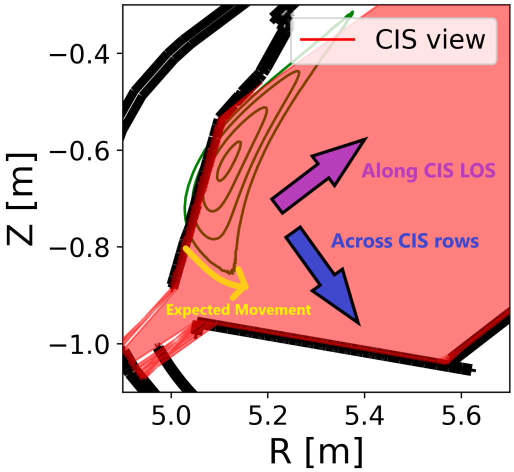

Figure 14: Field of view of the CIS diagnostic for a poloidal cross section at $\phi = 133.5°$, with arrows highlighting the directions along the CIS lines of sight and across the CIS rows. The island flux surfaces in standard configuration are shown in green. The black structure represents the projection of the target in the (R,Z) plane. The expected movement of the C III emission if it were to move off the target along the fieldlines is pictured in yellow.

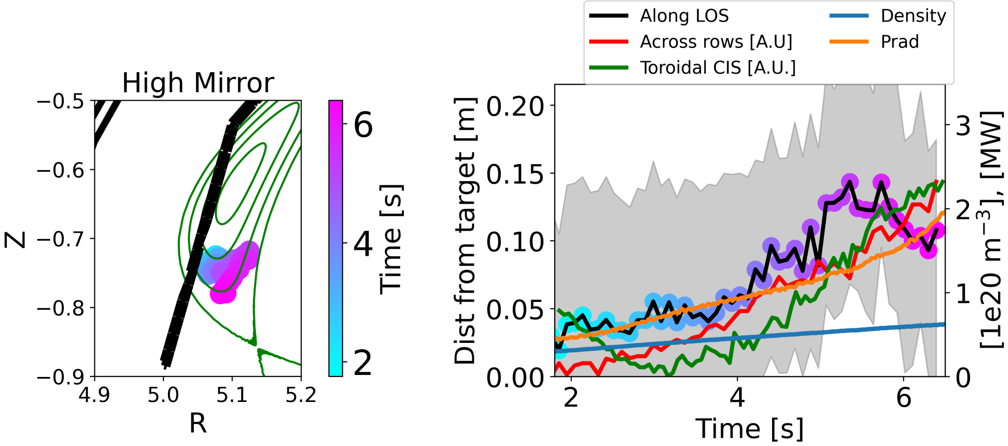

(a) (b)

Figure 15: Movement of the 25 % brightest pixels in the vertical target ROI for discharge #20230214.42 (high-mirror) and with inferred toroidal location in the interval [133.3, 133.8]°(a) projected in the (R,Z) plane and (b) as a trace. The target is shown in black and the island flux surfaces in green. Also shown are the line-averaged density, the radiated power, the movement of the peak brightness across image rows and the movement of the emission peak along the reference line in figure 11, both normalized with a minimum in 0 and maximum corresponding to the maximum value of the average MAP.

and in qualitative agreement with the emission movement across the camera rows and the one observed by the toroidal CIS system.

6 C III emission localization in density ramps to detachment

The inference can then be applied to slow core density ramps in the three magnetic configurations shown in section 1.1 to study the C III emission front location with increasing depth of detachment. Langmuir probes were unavailable during these discharges, thus a comparison with the ion flux roll-over is not possible. The results can instead be compared to the increasing radiated power measured by the bolometers and the movement of the emission across the multi-delay CIS camera rows and along the specified line of the toroidal CIS view in figure 11, as done in section 5.

6.1 High Mirror configuration

The inferred movement of the brightest emission band in the same region of interest as in fig 13a is shown for a line-averaged density ramp in high-mirror configuration (#20230214.42) in the poloidal plane and as a 1D trace in figure 15. The C III emission is inferred by CIS to be initially at the target, then slowly move away with increasing line-averaged density. The movement of the emission away from its initial position across the CIS camera rows and by the toroidal CIS system appears to coincide in time with the CIS inference of the emission movement away from the target, within the uncertainty bounds. This qualitative agreement seems to suggest that the current CIS setup is able to qualitatively distinguish between the emission being localized at the target or not. Interestingly, the upper part of the vertical target shows a secondary emission band. Its inferred location is shown using a dedicated red polygon mask and in the same toroidal interval as before in figure 16. Due to the uncertainty in the localization, it is difficult to determine if the emission is inferred to be at the target or near the O-point of the magnetic island at the start of the discharge, but with increasing line-averaged density it is observed to slowly move away through the island and towards

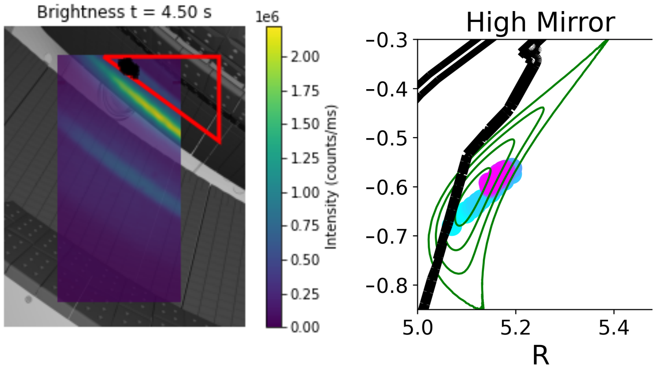

(a) (b)

Figure 16: (a) Region of interest for the emission band in the top of the vertical target(red). The 25% brightest pixels in the region of interest with inferred location in the toroidal range [133.3, 133.8]° are highlighted in black. (b) Movement of the 2nd emission band on the vertical target projected in the (R,Z) plane in discharge #20230214.42.

the separatrix in later stages of the discharge. More accurate inference of the movement of these bands may be obtained in the future with a more optimized CIS system.

6.2 Standard configuration

The behaviour in a line-averaged density ramp in the standard configuration (#20230209.30) is similar and it is shown for the main emission band on the vertical target in figure 17. In this case, the radial movement (along the lines of sight) inferred by multi-delay CIS appears to happen with a time delay with respect to the poloidal movement (along the camera rows), as within the uncertainty bounds the emission could be at the target up to 8 seconds into the discharge. This could be attributed to the lower C III emission near the vertical target leading to worse signal-to-noise ratio compared to the high-mirror case, or that a worse CIS performance is expected from standard configuration due to the smaller variation in magnetic field (figure 8). While the average distance from the target is already larger than 0 at the start of the discharge, the measurement is comparable with an attached divertor within uncertainty.

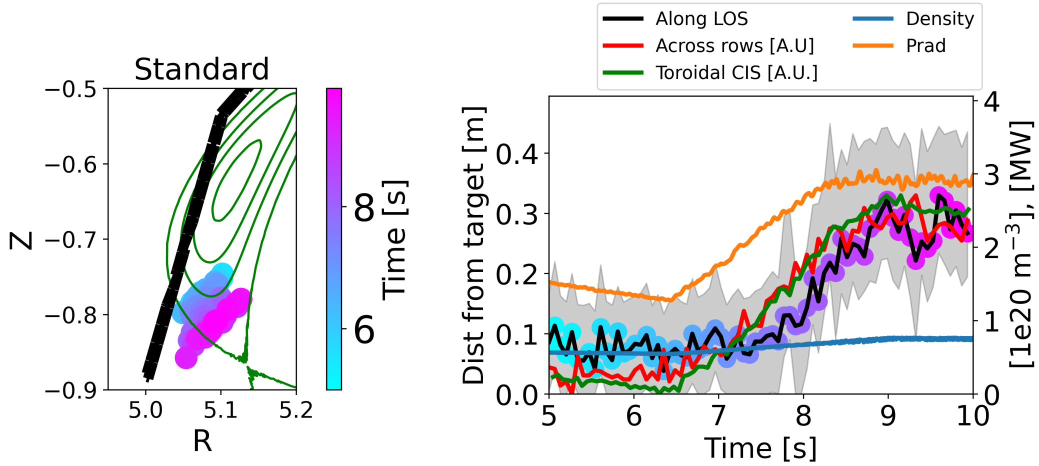

(a) (b)

Figure 17: Movement of the brightest region in the vertical target ROI for discharge #20230209.30 (a) projected in the (R,Z) plane and (b) as a trace for a core density ramp in standard configuration. Also shown are the line-averaged density, the radiated power, the movement of the peak brightness across image rows and the movement of the emission peak along the reference line in figure 11, both normalized with a minimum in 0 and maximum corresponding to the maximum value of the average MAP.

6.3 Low Iota configuration

In low-iota configuration (#20230125.018), most of the emission is on the horizontal target, complicating the inference on the vertical target. Even still, the emission is inferred to be initially attached at the target and then quickly move in two discrete steps at 6 and 8 seconds, as shown in figure 18. While before 6 s the inference is localized at the target and with smaller uncertainty, after 6 s there is a sharp transition and the uncertainty bounds cover most the island width. This is indicative of the detached state and consistent with a more distributed emission throughout the island. It could also be consistent with the camera averaging the signal over a fast oscillation of the emission location in the SOL in this configuration [26]. After 8 s, the emission is inferred to be more localized near the LCFS. The sharp movement is in qualitative agreement with the toroidal CIS view and consistent with the idea that detachment is highly sensitive in the low-iota configuration, as previously shown in modeling and experiments [26].

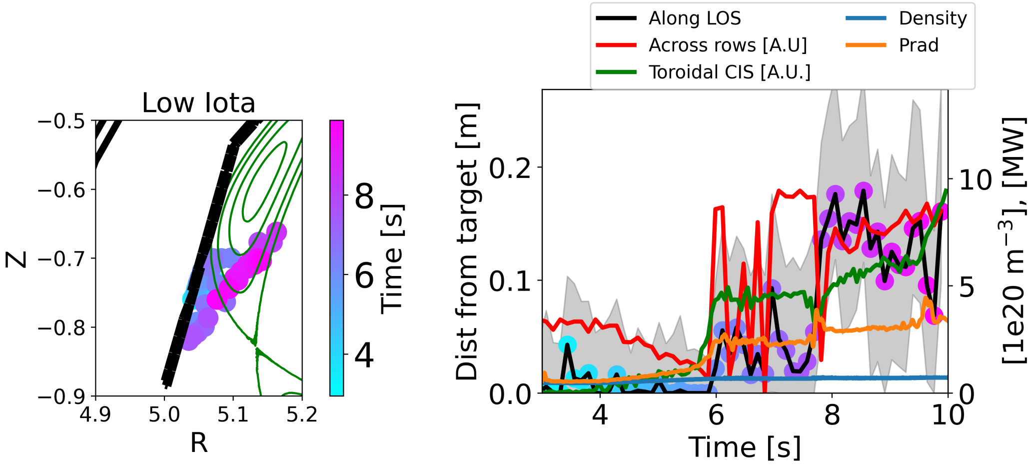

(a) (b)

Figure 18: Movement of the brightest pixels in the vertical target ROI for discharge #20230125.018 in low-iota configuration (a) projected in the (R,Z) plane and (b) as a trace. Also shown are the line-averaged density, the radiated power, the movement of the peak brightness across image rows and the movement of the emission peak along the reference line in figure 11, both normalized with a minimum in 0 and maximum corresponding to the maximum value of the average MAP.

6.4 Toridal variation in detachment threshold

The toroidal variation of the time at which the C III front detaches from the divertor can be studied by comparing 1D traces with different toroidal angle filters. The selected pixels and the respective 1D traces for toroidal intervals of 0.5° width centered at different toroidal angles are shown in figure 19. The inferred detachment time of the emission *along the line of sight* is seen to vary significantly with toroidal angle. The emission movement off the target is inferred to happen earliest for $\phi \sim 136°$ and latest for a toroidal angle of $\phi \sim 134°$. Given the large uncertainties, these results should be taken as qualitative, although more quantitative physics studies may be possible with a crystal setup optimized for these measurements. Future work could try to the project this movement to infer the increasing parallel distance along the fieldlines. Larger toroidal angles are not considered as the magnetic field gradient becomes small on the right part of the image (figure 9).

6.5 Spatial distribution of emission

As an example of other possible applications of the technique, the spatial distribution of the inferred emission for the vertical target ROI in attached and detached conditions for the main emission band

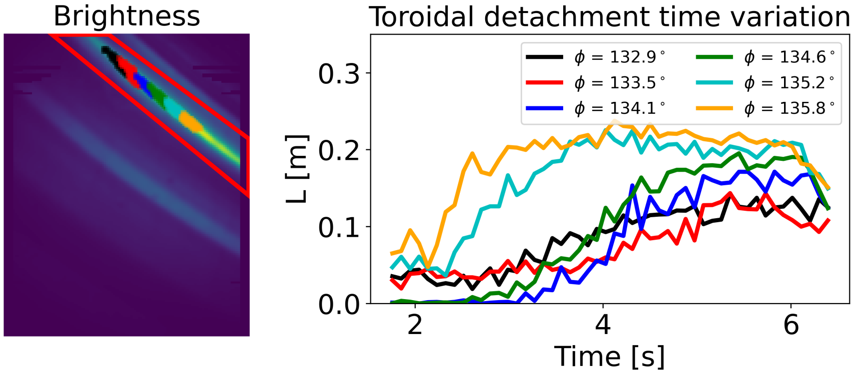

(a) (b)

Figure 19: (a) Selected pixels for different toroidal angle intervals and (b) corresponding 1D distance traces during the line-averaged density ramp in the high-mirror configuration #20230214.42.

on the vertical target is shown in figure 20 for the three magnetic configurations considered in this work. The C III emissivity spatial distributions are obtained as the sum of 2D gaussian distributions in the (R,Z) plane with standard deviation of 0.75 cm centered in the inferred location of all the filtered pixels (i.e. 25 % brightest pixels in the band with inferred location in [133.3, 133.8]°, such as the black pixels in figure 13). This process combines the (mostly poloidal) 2D information on the brightness measured by the different pixels with the (mostly radial) localization information along the line of sight of each pixel. In the presence of more accurate localization information across the entire image, 3D emissivity reconstructions in the entire observed toroidal interval could be possible with this approach.

In all three configurations, a significant difference is evident between attached and detached conditions. Generally, the emission is inferred to be more strongly localized at the target in attached conditions and more distributed throughout the SOL in strongly detached conditions.

7 Optimizing CIS for Zeeman localization

The current W7-X multi-delay system has 2 retarder crystals: a displacer plate (ϕ_1) and delay plate (ϕ_2). The former was designed to minimize the effect of Zeeman splitting on its contrast[6] and the latter was chosen among the crystals already available on site. Better localization performance can be obtained by choosing a delay plate that is optimized to maximize the dependence on Zeeman splitting. This can be performed by studying the variation of the second derivative of the log-likelihood with respect to the parameters characterizing the lineshape. The relation between plasma parameters and the likelihood depends on the group delay of the crystal, which is the parameter to be optimized [6]. Higher second derivatives will lead to more peaked probability distributions and thus lower uncertainty on the measurements. Furthermore, optimizing the derivatives of the log-likelihood, instead of the contrast directly, allows accounting for the assumptions made on the contrast uncertainty when considering multiple measurements simultaneously, as in a multi-delay design. In particular, minimizing the ratio of the second derivative with respect to temperature

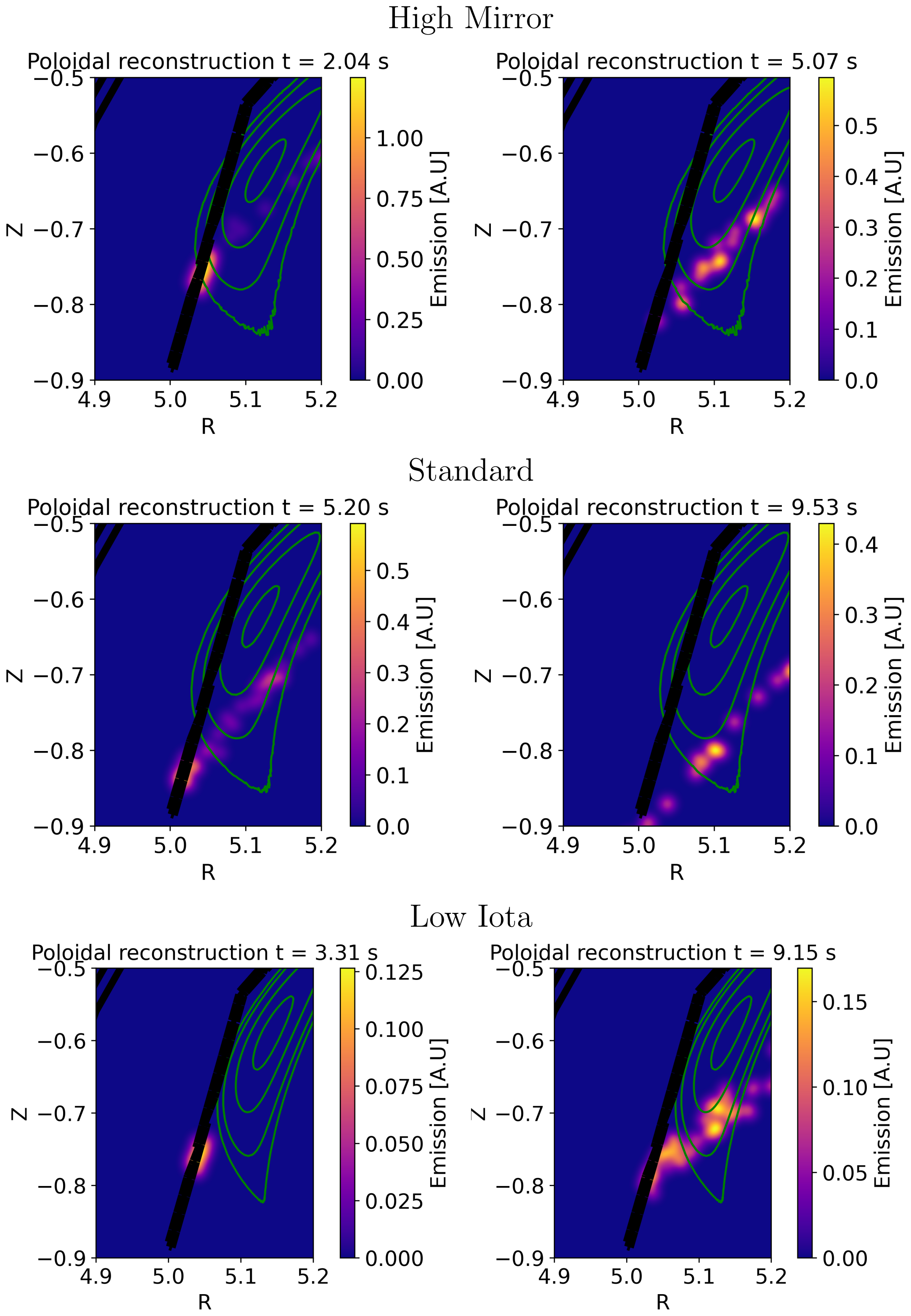

Figure 20: 2D spatial distribution of the C III emission for the main emission band on the vertical target in the toroidal range [133.3, 133.8]° in attached (left) and detached (right) conditions in the high-mirror, standard and low-iota configurations.

and the second derivative with respect to magnetic field strength

$$\min \left\{ \frac{\mathrm{d}^2 \log \mathcal{L}}{\mathrm{d}T^2} / \frac{\mathrm{d}^2 \log \mathcal{L}}{\mathrm{d}B^2} \right\} \tag{9}$$

can increase the relative sensitivity to Zeeman splitting. This ratio, obtained as an average in a representative parameter region for W7-X ($B \in [2, 3]$ T, $T_i \in [0, 50]$ eV, M $\in$ [0.9, 1.15]) is shown as a function of group delay in figure 21a. Minimizing the sum of the logarithms of this ratio for the $\phi_2, \phi_2 + \phi_1$ and $\phi_2 - \phi_1$ delays leads to a design interferometric delay of $\phi_2 = 820$ waves, compared to the current value of 1080 waves. This would lead to an increase in relative sensitivity to the magnetic field compared to the ion temperature of a factor 2.6x for $\phi_2 + \phi_1$ and 1.5x for $\phi_2 - \phi_1$. The relative sensitivity of the new crystals to varying multiplet enhancement factor (M) can also be explored, as these effects can alter the inferred values of interest. The ratio between the second derivative of the log-likelihood with respect to M and the second derivative with respect to B is shown as a function of group delay in figure 21b. With the new crystal set ϕ_2 would become significantly more sensitive to M (50x) compared to the magnetic field, while $\phi_1 + \phi_2$ and $\phi_2 - \phi_1$ become 2.3x and 1.15x more sensitive to the magnetic field with respect to M. To quantify the expected improvement with the new crystal, the 1D distance PDF resulting from synthetic measurements of an ideal instrument with the current crystal $\phi_2^C = 1080$ waves and with the optimized value $\phi_2^O = 820$ can be compared, as done in figure 22. The synthetic measurements are generated by assuming that the inferred MAP values in experiment for a single pixel of the camera view at different times during the discharge are correct, in order to use experimentally relevant parameters. The optimized crystals lead to significantly more peaked probability distributions, and thus a reduction in the expected uncertainty, as well as a more accurate estimate of the original value from the marginalized probability distribution. The optimized crystal has been procured and will be tested in future experiments.

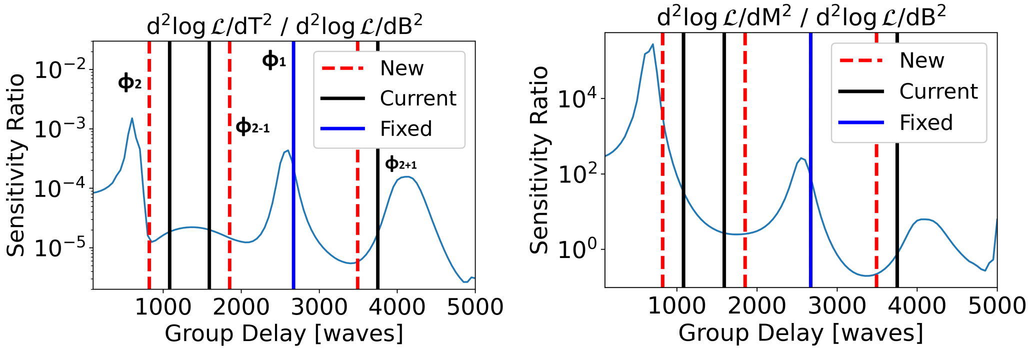

(a) (b)

Figure 21: Ratio of the second derivative of the log likelihood with respect to (a) temperature and (b) M over the second derivative with respect to magnetic field strength. The vertical black lines show the current delay values and the red lines the values for the optimized ϕ_2 delay of 820 waves. The blue line shows the ϕ_1 delay, already optimized for sensitivity to T_i.

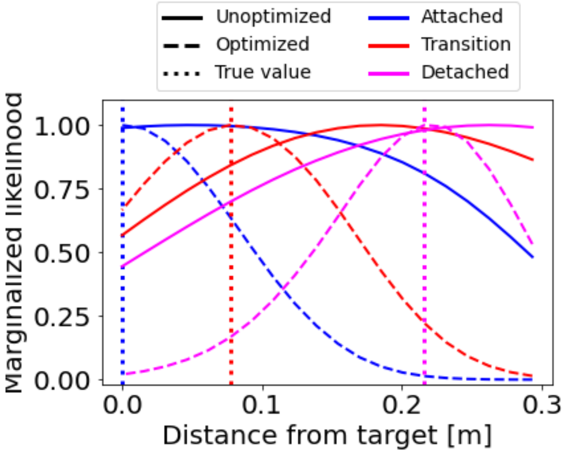

Figure 22: 1D Likelihoods for the distance inferred by an ideal instrument with the current setup (solid) and with the improved crystals (dashed) looking at the example pixel on the vertical target shown in green in figure 2. The vertical dotted lines show the correct values, which are experimental MAP values from the discharge in the high-mirror configuration (#20230214.42).

8 Conclusions

Multi-delay coherence imaging spectroscopy has been used to infer the location of the C III emission along the line of sight of each pixel over the 2D field of view of the camera. This can allow tracking the movement of the C III emission front away from the target during detachment with improved spatial resolution in both poloidal and toroidal directions compared to dispersive spectroscopy. The measurements, based on the effect of Zeeman splitting on the measured contrast, show the emission move away from the target as the divertor detaches in line-averaged density ramp discharges in standard, high-mirror and low-iota configurations in W7-X. The inference has been found to give reasonable results as a binary indicator for attached or detached conditions, in qualitative agreement with other diagnostics, although the inference of the precise location has large uncertainty in detached conditions. Reasonable performance is only found for the part of the image looking at the vertical target, possibly as the field variation between the last closed flux surface and the target is larger than for the pixels looking at the horizontal target. The time at which the emission is inferred to move away from the target can vary toroidally, highlighting the importance of imaging diagnostics in the study of non-axisymmetric machines. To improve the performance of the instrument, the optical properties of a set of crystals have been determined to optimize the W7-X diagnostic for this type of measurement. The new set-up is expected to lead to at least a doubling of the relative magnetic field sensitivity compared to the current system and a significant reduction in the localization uncertainty. The improved localization measurements could allow 3D reconstructions of the C III emission distribution in the divertor and good localization performance on the horizontal target as well. In turn, this could enable more detailed comparisons with modeling and more in-depth study of the physics driving the C III radiation movement.

9 Acknowledgements

This work has been carried out within the framework of the EUROfusion Consortium, partially funded by the European Union via the Euratom Research and Training Programme (Grant Agreement No 101052200 — EUROfusion), and from EPSRC Grant EP/S022430/1. Views and opinions expressed are however those of the author(s) only and do not necessarily reflect those of the European Union or the European Commission. Neither the European Union nor the European Commission can be held responsible for them.

Appendix A Last Closed Flux Surface - Target distance constraint

The magnetic field strength along the line of sight of the camera is non-monotonic. For example, it increases toward the core and then decreases toward the target. As most of the emission is expected near the target, the solution space can be constrained to only consider emission locations between the target and 10 cm inside the last closed flux surface (LCFS). This requires determining the location along the line of sight where the LCFS is intersected. Field line tracing is used to determine a set of points on the separatrix, which is then fitted with a 2D Fourier surface. The equation for the intersection of the 2D surface with the line of sight of each pixel is then solved numerically. The resulting distance between the target and the LCFS intersection is shown across the field of view for standard configuration in figure A1.

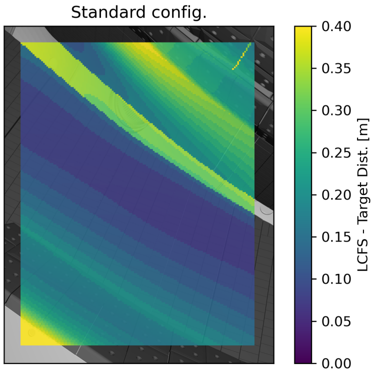

Figure A1: Target - LCFS distance along the line of sight of each pixel in standard configuration.

Appendix B Spectral model comparisons

The results of the inference for the high-mirror density ramp in the reference image slice are compared in figure B1 against two alternative spectral models:

- A model which assumes the expected statistical population distribution for the 3 components of the C III multiplet, thus with a three-dimensional parameter grid (v, T_i, L) and where M has been fixed to 1
- A model which includes a small fraction of emission coming from the oxygen OII spectral line at 465 nm, which also falls within the bandpass filter of the C III line. Here a five-dimensional

grid is used with variables (v, T_i, L, M, O) and the oxygen fraction is assumed to be between 0 and 10 % of the total emission. The ion temperature is assumed to be the same for the C III and OII line.

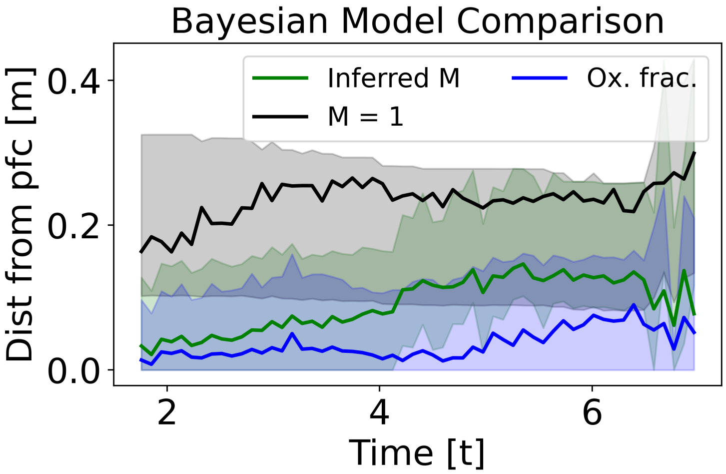

Figure B1: Comparison of the emission movement inferred by the 3D (M=1), 4D (Inferred M) and 5D (Ox. Frac.) bayesian models for the brightest emission band on the vertical target in high-mirror density ramp #20230214.42 and with inferred toroidal location in the interval [133.3, 133.8]°.

In the M = 1 model the emission is inferred to be always detached from the target, while in the model including oxygen the emission is inferred to detach later on in the discharge. More in general, enforcing $M = 1$ leads to the inferred magnetic field to be larger as Zeeman splitting must account for more of the reduction in contrast compared to the non-broadened case, and thus a larger distance from the target, while including the effect of oxygen leads to some of the reduction in contrast being due to the oxygen lines and thus a lower inferred magnetic field and more attached conditions inferred. The 4 dimensional grid (v, T_i, L, M) is used as the standard analysis routine for the discharges studied in the case as it is the model that agrees better with the movement of the C III emission in the poloidal direction and with the toroidal CIS system, both moving away from their initial positions at $t \approx 3$ s, as shown in figure 15. This suggests that the 4 contrast measurements do not contain enough spectral information to also infer the presence of small concentrations of oxygen impurities, as otherwise an improvement in the agreement with the other diagnostics would be expected.

References

[1] Linehan B L, Perek A, Duval B P, Bagnato F, Blanchard P, Colandrea C, Oliveira H D, Février O, Flom E, Gorno S, Goto M, Marmar E, Martinelli L, Mathews A, Muñoz-Burgos J, Mykytchuk D, Offeddu N, Oliveira D S, Reimerdes H, Reiter D, Schmitz O, Terry J L, Theiler C, Tsui C K, Vincent B, Wijkamp T, Wüthrich C, Zholobenko W and Team t T 2023 *Nuclear Fusion* **63** 036021 ISSN 0029-5515 publisher: IOP Publishing URL `https://dx.doi.org/10.1088/1741-4326/acb5b0`

[2] Greenhouse D, Bowman C, Lipschultz B, Verhaegh K, Harrison J R and Fil A 2025 *Plasma Physics and Controlled Fusion* URL `http://iopscience.iop.org/article/10.1088/1361-6587/adab1b`

[3] Perseo V, Effenberg F, Gradic D, König R, Ford O, Reimold F, Ennis D, Schmitz O, Pedersen T S and the W7-X Team 2019 *Nuclear Fusion* **59** 124003 URL `https://dx.doi.org/10.1088/1741-4326/ab4320`

[4] Perseo V, Gradic D, König R, Ford O P, Killer C, Grulke O, Ennis D A and Team W X 2020 *Review of Scientific Instruments* **91** ISSN 0034-6748 013501 URL `https://doi.org/10.1063/1.5126098`

[5] Lopez-Cansino R, Perseo V, Viezzer E, Kriete D M, Ford O P, Romba T, Poloskei P Z and the W7-X Team 2024 *Plasma Physics and Controlled Fusion* **66** 045012 URL `https://dx.doi.org/10.1088/1361-6587/ad290e`

[6] Kriete D M, Perseo V, Gradic D, Ennis D A, König R, Maurer D A and Team W X 2024 *Review of Scientific Instruments* **95** 073503 ISSN 0034-6748 URL `https://doi.org/10.1063/5.0208586`

[7] Verhaegh K, Lipschultz B, Harrison J, Osborne N, Williams A, Ryan P, Allcock J, Clark J, Federici F, Kool B, Wijkamp T, Fil A, Moulton D, Myatra O, Thornton A, Bosman T, Bowman C, Cunningham G, Duval B, Henderson S, Scannell R and the MAST Upgrade team 2022 *Nuclear Fusion* **63** 016014 URL `https://dx.doi.org/10.1088/1741-4326/aca10a`

[8] Verhaegh K, Lipschultz B, Harrison J, Federici F, Moulton D, Lonigro N, Kobussen S, O'Mullane M, Osborne N, Ryan P, Wijkamp T, Kool B, Rose E, Theiler C, Thornton A and the MAST Upgrade Team 2023 *Nuclear Fusion* **63** 126023 URL `https://dx.doi.org/10.1088/1741-4326/acf946`

[9] Verhaegh K, Harrison J, Lipschultz B, Lonigro N, Kobussen S, Moulton D, Osborne N, Ryan P, Theiler C, Wijkamp T, Brida D, Derks G, Doyle R, Federici F, Hakola A, Henderson S, Kool B, Newton S, Osawa R, Pope X, Reimerdes H, Vianello N, Wischmeier M, the EUROfusion Tokamak Exploitation Team and the MAST-U Team 2024 *Nuclear Fusion* **64** 086050 URL `https://dx.doi.org/10.1088/1741-4326/ad5851`

[10] Kool B, Verhaegh K, Derks G L, Wijkamp T A, Lonigro N, Doyle R, McArdle G, Vincent C, Lovell J, Federici F, Henderson S S, Osawa R T, Brida D, Reimerdes H, van Berkel M, tokamak exploitation team T E and the MAST-U team 2024 First demonstration of super-x divertor exhaust control for transient heat load management in compact fusion reactors (*Preprint* 2407.07784) URL `https://arxiv.org/abs/2407.07784`

[11] Ravensbergen T, van Berkel M, Perek A, Galperti C, Duval B P, Février O, van Kampen R J R, Felici F, Lammers J T, Theiler C, Schoukens J, Linehan B, Komm M, Henderson S, Brida D and de Baar M R 2021 *Nature Communications* **12** 1105 ISSN 2041-1723 publisher: Nature Publishing Group URL `https://www.nature.com/articles/s41467-021-21268-3`

[12] Theiler C, Lipschultz B, Harrison J, Labit B, Reimerdes H, Tsui C, Vijvers W, Boedo J A, Duval B, Elmore S, Innocente P, Kruezi U, Lunt T, Maurizio R, Nespoli F, Sheikh U, Thornton A, van Limpt S, Verhaegh K, Vianello N, the TCV team and the EUROfusion MST1 team 2017 *Nuclear Fusion* **57** 072008 URL `https://dx.doi.org/10.1088/1741-4326/aa5fb7`

[13] Wijkamp T A, Allcock J S, Feng X, Kool B, Lipschultz B, Verhaegh K, Duval B P, Harrison J R, Kogan L, Lonigro N, Perek A, Ryan P, Sharples R M, Classen I G J, Jaspers R J E and team t M U 2023 *Nuclear Fusion* **63** 056003 ISSN 0029-5515 publisher: IOP Publishing URL `https://dx.doi.org/10.1088/1741-4326/acc191`

[14] Perek A, Linehan B, Wensing M, Verhaegh K, Classen I, Duval B, Février O, Reimerdes H, Theiler C, Wijkamp T and de Baar M 2021 *Nuclear Materials and Energy* **26** 100858

[15] Pedersen T S, Otte M, Lazerson S, Helander P, Bozhenkov S, Biedermann C, Klinger T, Wolf R C and Bosch H S 2016 *Nature Communications* **7** 13493 ISSN 2041-1723 publisher: Nature Publishing Group URL `https://www.nature.com/articles/ncomms13493`

[16] Gradic D, Krychowiak M, König R, Henke F, Otte M, Perseo V, Pedersen T S and Team W X 2022 *Plasma Physics and Controlled Fusion* **64** 075010 ISSN 0741-3335 publisher: IOP Publishing URL `https://dx.doi.org/10.1088/1361-6587/ac70fa`

[17] Beidler C D, Smith H M, Alonso A, Andreeva T, Baldzuhn J, Beurskens M N A, Borchardt M, Bozhenkov S A, Brunner K J, Damm H, Drevlak M, Ford O P, Fuchert G, Geiger J, Helander P, Hergenhahn U, Hirsch M, Höfel U, Kazakov Y O, Kleiber R, Krychowiak M, Kwak S, Langenberg A, Laqua H P, Neuner U, Pablant N A, Pasch E, Pavone A, Pedersen T S, Rahbarnia K, Schilling J, Scott E R, Stange T, Svensson J, Thomsen H, Turkin Y, Warmer F, Wolf R C and Zhang D 2021 *Nature* **596** 221–226 ISSN 1476-4687 publisher: Nature Publishing Group URL `https://www.nature.com/articles/s41586-021-03687-w`

[18] Pedersen T S, Abramovic I, Agostinetti P, Torres M A, Äkäslompolo S, Belloso J A, Aleynikov P, Aleynikova K, Alhashimi M, Ali A, Allen N, Alonso A, Anda G, Andreeva T, Angioni C, Arkhipov A, Arnold A, Asad W, Ascasibar E, Aumeunier M H, Avramidis K, Aymerich E, Baek S G, Bähner J, Baillod A, Balden M, Balden M, Baldzuhn J, Ballinger S, Banduch M, Bannmann S, Navarro A B, Navarro A B, Barbui T, Beidler C, Belafdil C, Bencze A, Benndorf A, Beurskens M, Biedermann C, Biletskyi O, Blackwell B, Blatzheim M, Bluhm T, Böckenhoff D, Bongiovi G, Borchardt M, Borodin D, Boscary J, Bosch H, Bosmann T, Böswirth B, Böttger L, Bottino A, Bozhenkov S, Brakel R, Brandt C, Bräuer T, Braune H, Brezinsek S, Brunner K, Buller S, Burhenn R, Bussiahn R, Buttenschön B, Buzás A, Bykov V, Calvo I, Mata K C, Caminal I, Cannas B, Cappa A, Carls A, Carovani F, Carr M, Carralero D, Carvalho B, Casas J, Castano-Bardawil D, Castejon F, Chaudhary N, Chelis I, Chomiczewska A, Coenen J, Cole M, Cordella F, Corre Y, Crombe K, Cseh G,

Csillag B, Damm H, Day C, de Baar M, la Cal E D, Degenkolbe S, Demby A, Denk S, Dhard C, Siena A D, Dinklage A, Dittmar T, Dreval M, Drevlak M, Drewelow P, Drews P, Dunai D, Edlund E, Effenberg F, Ehrke G, Endler M, Ennis D, Escoto F, Estrada T, Fable E, Fahrenkamp N, Fanni A, Faustin J, Fellinger J, Feng Y, Figacz W, Flom E, Ford O, Fornal T, Frerichs H, Freundt S, Fuchert G, Fukuyama M, Füllenbach F, Gantenbein G, Gao Y, Garcia K, Regaña J G, García-Cortés I, Gaspar J, Gates D, Geiger J, Geiger B, Giudicotti L, González A, Goriaev A, Gradic D, Grahl M, Graves J, Green J, Grelier E, Greuner H, Groß S, Grote H, Groth M, Gruca M, Grulke O, Grün M, Arnaiz J G, Günter S, Haak V, Haas M, Hacker P, Hakola A, Hallenbert A, Hammond K, Han X, Hansen S, Harris J, Hartfuß H, Hartmann D, Hathiramani D, Hatzky R, Hawke J, Hegedus S, Hein B, Heinemann B, Helander P, Henneberg S, Hergenhahn U, Hidalgo C, Hindenlang F, Hirsch M, Höfel U, Hollfeld K, Holtz A, Hopf D, Höschen D, Houry M, Howard J, Huang X, Hubeny M, Hudson S, Ida K, Igitkhanov Y, Igochine V, Illy S, Ionita-Schrittwieser C, Isobe M, Jabłczyńska M, Jablonski S, Jagielski B, Jakubowski M, van Vuuren A J, Jelonnek J, Jenko F, Jenko F, Jensen T, Jenzsch H, Junghanns P, Kaczmarczyk J, Kallmeyer J, Kamionka U, Kandler M, Kasilov S, Kazakov Y, Kennedy D, Kharwandikar A, Khokhlov M, Kiefer C, Killer C, Kirschner A, Kleiber R, Klinger T, Klose S, Knauer J, Knieps A, Köchl F, Kocsis G, Kolesnichenko Y, Könies A, König R, Kontula J, Kornejew P, Koschinsky J, Kozulia M, Krämer-Flecken A, Krampitz R, Krause M, Krawczyk N, Kremeyer T, Krier L, Kriete D, Krychowiak M, Ksiazek I, Kubkowska M, Kuczynski M, Kühner G, Kumar A, Kurki-Suonio T, Kwak S, Landreman M, Lang P, Langenberg A, Laqua H, Laqua H, Laube R, Lazerson S, Lewerentz M, Li C, Liang Y, Linsmeier C, Lion J, Litnovsky A, Liu S, Lobsien J, Loizu J, Lore J, Lorenz A, Losada U, Louche F, Lunsford R, Lutsenko V, Machielsen M, Mackel F, Maisano-Brown J, Maj O, Makowski D, Manduchi G, Maragkoudakis E, Marchuk O, Marsen S, Martines E, Martinez-Fernandez J, Marushchenko M, Masuzaki S, Maurer D, Mayer M, McCarthy K, Mccormack O, McNeely P, Meister H, Mendelevitch B, Mendes S, Merlo A, Messian A, Mielczarek A, Mishchenko O, Missal B, Mitteau R, Moiseenko V, Mollen A, Moncada V, Mönnich T, Morisaki T, Moseev D, Motojima G, Mulas S, Mulsow M, Nagel M, Naujoks D, Naulin V, Neelis T, Neilson H, Neu R, Neubauer O, Neuner U, Nicolai D, Nielsen S, Niemann H, Nishiza T, Nishizawa T, Nishizawa T, Nührenberg C, Ochoukov R, Oelmann J, Offermanns G, Ogawa K, Okamura S, Ölmanns J, Ongena J, Oosterbeek J, Otte M, Pablant N, Alvarez N P, Alvarez N P, Pandey A, Pasch E, Pavlichenko R, Pavone A, Pawelec E, Pechstein G, Pelka G, Perseo V, Peterson B, Pilopp D, Pingel S, Pisano F, Plöckl B, Plunk G, Pölöskei P, Pompe B, Popov A, Porkolab M, Proll J, Pueschel M, Puiatti M E, Sitjes A P, Purps F, Rahbarnia K, Rasiński M, Rasmussen J, Reiman A, Reimold F, Reisner M, Reiter D, Richou M, Riedl R, Riemann J, Riße K, Roberg-Clark G, Rohde V, Romazanov J, Rondeshagen D, Rong P, Rudischhauser L, Rummel T, Rummel K, Runov A, Rust N, Ryc L, Salembier P, Salewski M, Sanchez E, Satake S, Satheeswaran G, Schacht J, Scharff E, Schauer F, Schilling J, Schlisio G, Schmid K, Schmitt J, Schmitz O, Schneider W, Schneider M, Schneider P, Schrittwieser R, Schröder T, Schröder M, Schroeder R, Schweer B, Schwörer D, Scott E, Scott E, Shanahan B, Sias G, Sichta P, Singer M, Sinha P, Sipliä S, Slaby C, Sleczka M, Smith H, Smoniewski J, Sonnendrücker E, Spolaore M, Spring A, Stadler R, Stańczak D, Stange T, Stepanov I, Stephey L, Stober J, Stroth U, Strumberger E, Suzuki C, Suzuki Y, Svensson J, Szabolics T, Szepesi T, Szücs M, Tabarés F, Tamura N, Tancetti A, Tantos C, Terry J, Thienpondt H, Thomsen H, Thumm M, Travere J, Traverso P, Tretter J, Trier E, Mora H T, Tsujimura T, Turkin Y, Tykhyi A, Unterberg B, van Eeten P, van Milligen B, van Schoor M, Vano L, Varoutis S, Vecsei M, Vela L, Velasco J, Vervier M, Vianello N, Viebke H, Vilbrandt R, Vogel G, Vogt N, Volkhausen C, von Stechow A, Wagner F, Wang E, Wang H, Warmer F, Wauters T, Wegener L, Wegner T, Weir G, Wenzel U, White A, Wilde F, Wilms F, Windisch T, Winkler M, Winter A, Winters V, Wolf R, Wright A, Wurden G, Xanthopoulos P, Xu S, Yamada H, Yamaguchi H, Yokoyama M, Yoshinuma M, Yu Q, Zamanov M, Zanini M, Zarnstorff M, Zhang D, Zhou S, Zhu J, Zhu C, Zilker M, Zocco A, Zohm H, Zoletnik S and Zsuga L 2022 *Nuclear Fusion* **62** 042022 URL `https://dx.doi.org/10.1088/1741-4326/ac2cf5`

[19] Schmitz O, Feng Y, Jakubowski M, König R, Krychowiak M, Otte M, Reimold F, Barbui T, Biedermann C, Bozhenkov S, Brezinsek S, Buttenschön B, Brunner K, Drewelow P, Effenberg F, Flom E, Frerichs H, Ford O, Fuchert G, Gao Y, Gradic D, Grulke O, Hammond K C, Hergenhahn U, Höfel U, Knauer J, Kornejew P, Kremeyer T, Niemann H, Pasch E, Pavone A, Perseo V, Rudischhauser L, Schlisio G, Sunn Pedersen T, Wenzel U, Winters V, Wurden G, Zhang D and W7-X team t 2020 *Nuclear Fusion* **61** 016026 URL `https://dx.doi.org/10.1088/1741-4326/abb51e`

[20] Gradic D, Perseo V, König R and Ennis D 2019 *Fusion Engineering and Design* **146** 995–998 ISSN 0920-3796 sI:SOFT-30 URL `https://www.sciencedirect.com/science/article/pii/S0920379619301565`

[21] Doyle R S, Lonigro N, Allcock J S, Silburn S A, Turner M M, Feng X and Leggate H 2024 *Review of Scientific Instruments* **95** 053505 ISSN 0034-6748 URL `https://doi.org/10.1063/5.0205584`

[22] Allcock J S, Silburn S A, Sharples R M, Harrison J R, Conway N J and Vernimmen J W M 2021 *Review of Scientific Instruments* **92** ISSN 0034-6748 073506 URL `https://doi.org/10.1063/5.0050704`

[23] Lonigro N, Doyle R S, Allcock J S, Lipschultz B, Verhaegh K, Bowman C, Brida D, Harrison J, Myatra O, Silburn S, Theiler C, Wijkamp T A, Team M U and the EUROfusion Tokamak Exploitation Team 2025 *Plasma Physics and Controlled Fusion* **67** 035003 URL `https://dx.doi.org/10.1088/1361-6587/adad97`

[24] Feng Y, Jakubowski M, König R, Krychowiak M, Otte M, Reimold F, Reiter D, Schmitz O, Zhang D, Beidler C, Biedermann C, Bozhenkov S, Brunner K, Dinklage A, Drewelow P, Effenberg F, Endler M, Fuchert G, Gao Y, Geiger J, Hammond K, Helander P, Killer C, Knauer J, Kremeyer T, Pasch E, Rudischhauser L, Schlisio G, Sunn Pedersen T, Wenzel U, Winters V and team W X 2021 *Nuclear Fusion* **61** 086012 URL `https://dx.doi.org/10.1088/1741-4326/ac0772`

[25] Zhang D, Burhenn R, Koenig R, Giannone L, Grodzki P A, Klein B, Grosser K, Baldzuhn J, Ewert K, Erckmann V, Hirsch M, Laqua H P and Oosterbeek J W 2010 *Review of Scientific Instruments* **81** 10E134 ISSN 0034-6748 (*Preprint* `https://pubs.aip.org/aip/rsi/article-pdf/doi/10.1063/1.3483194/15937464/10e134_1_online.pdf`) URL `https://doi.org/10.1063/1.3483194`

[26] Winters V, Reimold F, Feng Y, Zhang D, Perseo V, Flom E, Henke F, Kriete D, Maaziz N, Partesotti G, Jakubowski M, König R, Krychowiak M, Brunner K, Knauer J, Rahbarnia K and the W7-X Team 2024 *Nuclear Fusion* **64** 126047 URL `https://dx.doi.org/10.1088/1741-4326/ad820e`